ARTICLE

Exsolution of Fe-Ni alloy nanoparticles from (La,Sr)(Cr,Fe,Ni)O_3 perovskites as potential Oxygen Transport Membrane catalysts for methane reforming

Received 00th January 20xx,
Accepted 00th January 20xx

DOI: 10.1039/x0xx00000x

Despoina Papargyriou, [a] David Miller [a] and John Thomas Sirr Irvine* [a]

$(La_{0.75}Sr_{0.25})(Cr_{0.5}Fe_{0.5-x}Ni_x)O_3$ perovskites were investigated as potential catalysts for Oxygen Transport Membranes for methane reforming applications. XRD was performed to study the structural changes that take place when Fe was partially substituted by Ni, in both oxidising and reducing environments. TGA measurements demonstrated the oxygen deficiency of these perovskites in reducing conditions was enhanced by increasing the level of Ni doping, due the reduction of the Fe^{3+}/Fe^{4+} and Ni^{2+} species to lower cation valences. SEM and TEM-EDX analyses showed upon reduction exsolution of bimetallic Fe-Ni alloy nanoparticles took place on the surface of the perovskite, which was beneficial for the catalyst's activity. The optimum stoichiometry was the $(La_{0.75}Sr_{0.25})(Cr_{0.5}Fe_{0.35}Ni_{0.15})O_3$ perovskite, which during catalytic testing, demonstrated 72% CH_4 conversion, that was 20 times higher than that of the initial perovskite.

Introduction

Oxygen Transport Membranes (OTMs) have been the subject of research in recent years as they can efficiently separate oxygen from air and reduce the cost of processes that require pure oxygen.[1–3] The application of OTMs for syngas production from natural gas and other hydrocarbon sources has attracted a lot of attention. The use of dense ceramic membranes with mixed oxygen-ionic and electronic conductivity, makes it possible to combine oxygen separation from air, partial oxidation of methane and reforming, in a single reactor.[4]

One important aspect of membrane material development is the enhancement of their catalytic performance. For this purpose, a lot of scientists have investigated the influence of the addition of a catalyst, as an exchange layer in the fuel side of the OTMs, in order to improve the surface exchange kinetics and thus, the oxygen flux. In general, the most commonly used catalysts for methane reforming in OTMs are the Ni supported catalysts.[5–8] Ni has the ability to easily break the C-H bond and activate the CH_4 molecule for partial oxidation reactions. Moreover, when applied for OTM processes, Ni helps maintain the oxygen chemical potential driving force across the membrane by consuming the oxygen that is transported.[9,10] Furthermore, a lot of attention has been drawn to perovskites, since they can accelerate the oxygen reduction and therefore improve the incorporation of oxygen ions on the surface of the OTM.[11–13] This process is similar to the solid oxide fuel cell operation and with the addition of a metal catalyst, perovskites are very promising candidate materials as catalysts for OTMs.[10] Here we investigate $(La_{0.75}Sr_{0.25})(Cr_{0.5}Fe_{0.5})O_3$ perovskites as potential materials for the catalytic layer of OTMs. These materials demonstrate good chemical and mechanical stability under membrane's operating conditions, compatibility with the interconnect materials of the membrane, high electronic and ionic conductivity and good catalytic activity for methane reforming reactions.[14,15]

To further improve the catalytic activity of these perovskites and consequently the OTM's performance, the incorporation of metal nanoparticles is investigated.[16] Generally, several deposition techniques such as physical vapor deposition and chemical impregnation have been used to form metal nanoparticles on oxide supports for catalytic applications.[17,18] However, these techniques are difficult to perform in the OTM system, as the catalytic layer is deeply buried in the OTM structure.[19] Moreover, the nanoparticles formed by deposition techniques often suffer from agglomerations due to weak interaction with the oxide support.[17,20]

To overcome these issues, *in-situ* nanocatalyst exsolution has emerged recently as an alternative procedure. This method allows the growth of metal nanoparticles from the perovskite lattice on its surface through a single reduction step.[21] A good control of the nanoparticle size and distribution[20] and the regeneration of the nanostructure *via* a redox cycle[22,23] can be achieved by this technique. Moreover, these exsolved nanoparticles demonstrate very good thermal stability and good anti-coking behaviour, due to their strong interaction with the parent perovskite.[20] Finally, several studies have shown the exsolution of metal nanoparticles from the B-site of the perovskites offers better electrocatalytic properties, when tested in fuel cells, electrolysis cells and for automotive emission control.[24–26]

[a] *School of Chemistry, University of St Andrews, Fife, KY16 9ST, UK*
Email: jtsi@st-andrews.ac.uk

Electronic Supplementary Information (ESI) available: [Additional graphs of the thermodynamic equilibrium and blank test for the catalytic testing, TGA data during the redox cycle, additional SEM and TEM analyses of the exsolved samples]. See DOI: 10.1039/x0xx00000x

In this study, a series of $(La_{0.75}Sr_{0.25})(Cr_{0.5}Fe_{0.5-x}Ni_x)O_3$ perovskites is investigated as potential materials for the catalytic layer of OTMs. The influence of nanoparticles exsolution from this perovskite on its catalytic activity is evaluated and the most promising stoichiometry for the catalytic layer of the OTM is identified.

Experimental section

Synthesis of the materials

The $(La_{0.75}Sr_{0.25})(Cr_{0.5}Fe_{0.5-x}Ni_x)O_3$ perovskites were synthesised *via* a modified combustion synthesis with citric acid and ethylene glycol.[27] The precursors used for this synthesis were $La(NO_3)_3{\cdot}6H_2O$, $Sr(NO_3)_2$, $Cr(NO_3)_3{\cdot}9H_2O$, $Fe(NO_3)_3{\cdot}9H_2O$ and $Ni(NO_3)_2{\cdot}6H_2O$. These metal nitrates were diluted in distilled water in appropriate stoichiometric ratios. Citric acid and ethylene glycol were mixed with the metal nitrate solution under magnetic stirring at room temperature. Once total dissolution was achieved, the temperature was increased to 90-100 °C. The solution was stirred, until a swelling gel formed. Then, the temperature was gradually increased to 300 °C and the gel combusted in air forming a dark brown powder. The obtained powders were calcined in air at 1300 °C for 4 h, to obtain a single-phase perovskite structure. The samples were reduced in a tube furnace under 5% H_2/Ar at 900 °C for 20 h, to exsolve the metal nanoparticles on the surface of the perovskites. Table 1 presents the stoichiometry of the perovskites synthesised in this work and their corresponding abbreviations.

Characterisation techniques

Room temperature powder X-ray diffraction (XRD) was performed on a PANalytical Empyrean diffractometer operated in reflection mode using Cu-Kα1 radiation. The obtained XRD patterns were analysed with STOE WinXPOW software to determine the phase purity, crystal structure and cell parameters of the perovskites after different treatments. Thermogravimetric analysis (TGA) was conducted using a Netzsch STA 449C instrument equipped with Proteus thermal analysis software. The morphology of the samples surface was analysed using a JEOL JSM-6700 field emission 74 scanning electron microscope (FEG-SEM). Higher resolution imaging of the exsolved nanoparticles was conducted with a FEI Titan Themis Transmission Electron Microscope (TEM) fitted with an Oxford ISIS EDX system for elemental analysis.

Table 1 Stoichiometry of the synthesised perovskites and their abbreviations

Compound Stoichiometry	Abbreviation
$(La_{0.75}Sr_{0.25})(Cr_{0.5}Fe_{0.5})O_3$	LSCF
$(La_{0.75}Sr_{0.25})(Cr_{0.5}Fe_{0.47}Ni_{0.03})O_3$	LSCFNi3
$(La_{0.75}Sr_{0.25})(Cr_{0.5}Fe_{0.45}Ni_{0.05})O_3$	LSCFNi5
$(La_{0.75}Sr_{0.25})(Cr_{0.5}Fe_{0.40}Ni_{0.10})O_3$	LSCFNi10
$(La_{0.75}Sr_{0.25})(Cr_{0.5}Fe_{0.35}Ni_{0.15})O_3$	LSCFNi15
$(La_{0.75}Sr_{0.25})(Cr_{0.5}Fe_{0.30}Ni_{0.20})O_3$	LSCFNi20

Catalytic Testing

For the catalytic testing of the synthesised materials, a premixed gas of 12.9% CH_4, 25.8% CO_2 and 61.3% H_2 was used. This gas was humidified through a water bubbler at room temperature, to obtain 3% of steam in the gas stream. This gas composition was selected to replicate the gas feed of an OTM used in industry. It corresponds to the exhaust of a coal gasification unit.[3] Typically, this exhaust gas is fed to the OTM to generate syngas from the unreacted hydrocarbons.[3]

Figure 1 shows the experimental set-up used for testing the catalytic activity of the synthesised materials. The flow of the premixed gas was controlled with an Aalborg mass flow controller that was calibrated for the humidified gas mixture in the range of 0-50 ml/min. The reactor was placed in a microfurnace, which had a heating capacity of up to 950 °C. An internal thermocouple was placed close to the catalyst bed to monitor the exact temperature of each experiment. The outlet of the reactor was channelled to a water trap with a peltier cooler to condense any water from the gas stream. Then, the outlet gas was fed to a Gas Chromatograph (GC) for analysis. The GC was equipped with a HP-PLOT carbon plot column and was used to separate the H_2, CO, CO_2 and CH_4, with He as a carrier gas.

To maintain a reducing environment during heating and cooling, a 5% H_2/Ar gas mixture was used. When the desirable temperature was achieved, the premixed gas was introduced into the reactor and the evolution of the reaction products was monitored by the GC.

The configuration of the fixed-bed reactor used in these experiments is also illustrated in Figure 1. A tubular quartz microreactor, with internal diameter of 8 mm, external diameter of 10 mm and length 30 cm was used. For each experiment, 300 mg of catalyst was used, and the height of the catalyst bed was approximately 5 mm. All the samples were tested as powders and were supported between quartz wool plugs, with porosity between 5 to 30 µm. The space velocity used for these experiments was approximately 6000 h^{-1} and the temperature was maintained at 900 °C. This temperature falls within the range of the operating temperature of the OTMs (900 -1000 °C).

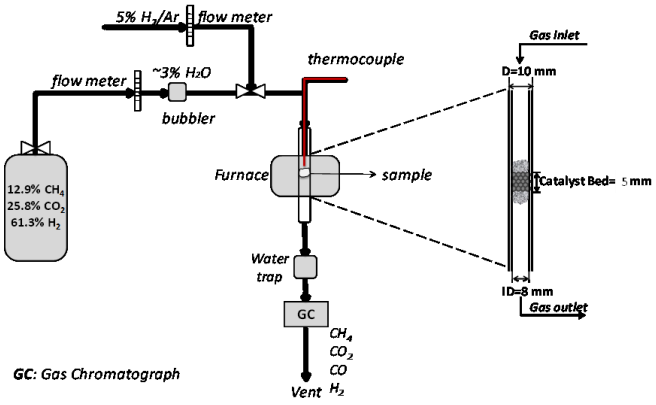

Figure 1 Flow diagram of the set up used for the catalytic experiments

The main reactions expected to take place at the OTM's operating temperate are methane steam reforming (Eq. 1), methane dry reforming (Eq. 2) and the reverse water-gas shift reaction (Eq. 3).

$$CH_4 + H_2O \rightarrow CO + 3H_2 \quad (1)$$

$$CH_4 + CO_2 \rightarrow 2CO + 2H_2 \quad (2)$$

$$CO_2 + H_2 \leftrightarrow CO + H_2O \quad (3)$$

The performance of the catalysts used in this work was evaluated based on the CH_4 and CO_2 conversion to gaseous products such as CO and H_2. These conversions were calculated according to the following equations based on the gas concentrations from the inlet and outlet of the reactor.

$$C_{CH4} = \frac{CH_4 in - CH_4 out}{CH_4 in} \cdot 100 \quad (4)$$

$$C_{CO2} = \frac{CO_2 in - CO_2 out}{CO_2 in} \cdot 100 \quad (5)$$

The thermodynamic equilibrium for the used gas composition was calculated with the HSC Chemistry software at 900 °C and 1 atm. According to the thermodynamic equilibrium, full CH_4 conversion and 90% CO_2 conversion are expected (Figure S1a). Finally, a blank catalytic test was performed at 900 °C with 6000 h^{-1} space velocity. When no catalyst was present (Figure S1b), the CH_4 concentration remained constant, indicating that CH_4 did not participate in any reaction. However, the CO_2 and H_2 concentrations decreased, while the CO and H_2O increased. This indicated that the reverse water-gas shift reaction took place in the gas phase to a small extent, according to Eq. 3. Therefore, to reach the thermodynamic equilibrium, the addition of a catalyst was necessary.

Results and Discussion

Crystal structure of the as-prepared and reduced perovskites

As-prepared perovskites. The partial substitution of Fe by Ni in the $(La_{0.75}Sr_{0.25})(Cr_{0.5}Fe_{0.5})O_3$ perovskite was investigated and the solubility limit of Ni on the B-site of the perovskite was determined by XRD analysis. The XRD patterns of the synthesised materials after calcination at 1300 °C for 4 h are presented in Figure 2. According to the literature, LSCF exhibits an orthorhombic structure with *Pnma* space group.[15] After partially substituting Fe with 3-5 mol% of Ni on the B-site of LSCF, the perovskite retained its orthorhombic structure. However, when the Ni doping was increased to 10-20 mol%, the symmetry of the perovskite changed to rhombohedral, with *R-3c* space group. Moreover, as shown in Figure 2a, for Ni doping of 20 mol%, a peak corresponding to unreacted NiO was observed, indicating that the solubility limit of Ni on the B-site of LSCF was between 15 and 20 mol%.

A magnified section of the XRD pattern (32-33 °) is given in Figure 2b. This shows the (020) and (112) reflections which correspond to the orthorhombic structure and the (110) and (104) reflections which correspond to the rhombohedral structure and illustrates the phase transition between 5 and 10 mol% of Ni doping on LSCF. In addition to that, these reflections showed a gradual shift to higher 2θ angles, when the Ni doping was increased. This suggests that the unit cell volume of the perovskite reduced when Ni partially substituted Fe.

Assuming the oxygen content is maintained, this cell contraction was attributed to a change in the oxidation states of Fe in LSCF when it was partially substituted by Ni. More specifically, in LSCF the oxidation state of Fe is a mixture of both Fe^{3+} (0.645Å) and Fe^{4+} (0.585Å).[15,28,29] When Ni^{2+} (0.69 Å) was incorporated into the structure, considering its ionic radius which is larger than that of Fe^{3+} and Fe^{4+},[29] an increase in the unit cell volume was expected. However, to maintain the charge balance, when Ni^{2+} is incorporated into the structure, Fe tends to obtain the +4 oxidation state, causing a decrease in the cell volume. Similar tendencies have been reported in the literature before for the $(La_{0.75}Sr_{0.25})(Cr_{0.5}Mn_{0.5})O_3$ perovskite by Jardiel *et al*. The authors have observed a decrease in the unit cell volume of the perovskite when increasing the Ni doping, due to changes in the oxidation state of Mn on the B-site.[30]

The unit cell parameters of the synthesised LSCF compounds are presented in Table 2. The pseudocubic cell volume was

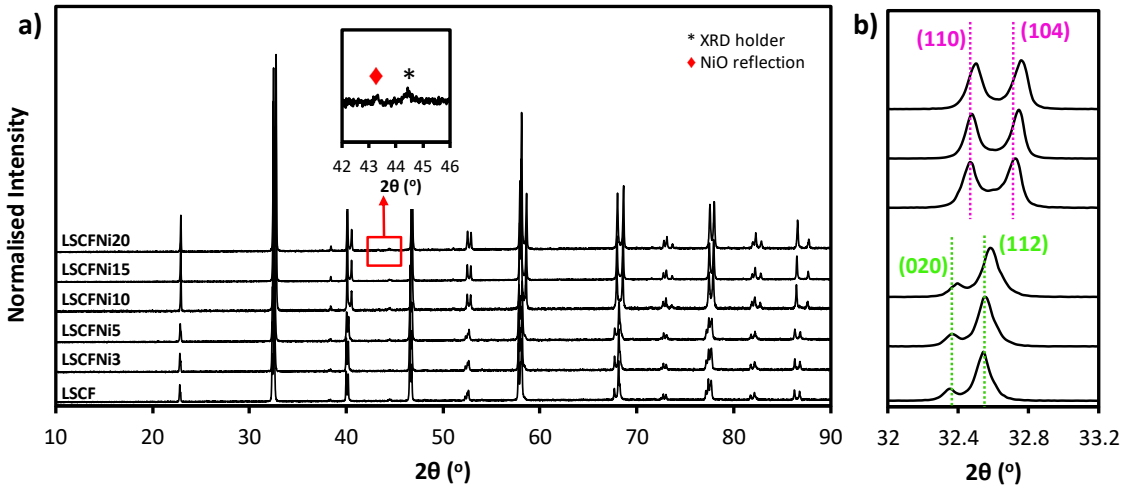

Figure 2 a) Room temperature XRD patterns of the LSCFNi perovskites b) Magnified section of the room temperature XRD patterns

Table 2 Unit cell parameters of the as-prepared LSCFNi perovskites

	LSCF	LSCFNi3	LSCFNi5	LSCFNi10	LSCFNi15	LSCFNi20
Space Group	*Pnma*	*Pnma*	*Pnma*	*R-3c*	*R-3c*	*R-3c*
a (Å)	5.4925(4)	5.4890(8)	5.4866(13)	5.5196(4)	5.5148(3)	5.5105(3)
b (Å)	5.5326(3)	5.5319(6)	5.5301(7)	-	-	-
c (Å)	7.7645(6)	7.7647(12)	7.7621(14)	13.3600(6)	13.3465(4)	13.3383(6)
Volume (Å^3)	235.95(2)	235.77(7)	235.51(5)	352.50(5)	351.53(3)	350.77(4)
Va (Å^3)	58.95	58.94	58.88	58.75	58.59	58.46

calculated to compare the change in the unit cell size for the LSCF with the different Ni doping. This confirms that the unit cell of the perovskite contracted when the Ni doping on the B-site of LSCF increased.

Reduction of the perovskites. Room temperature XRD patterns were collected on the LSCFNi compounds after reduction in 5% H_2/Ar for 20 h, to investigate any changes in the crystal structure of the perovskites after this treatment. The post-reduction XRD patterns are presented in Figure 3. LSCF has previously shown to undergo a phase transition from an orthorhombic to rhombohedral structure upon reduction.[15] Similar to LSCF, for LSCFNi3 and LSCFNi5 the crystal structure changed from orthorhombic to rhombohedral with *R-3c* space group. However, the LSCF samples with Ni doping greater than 10 mol%, which exhibited an initial rhombohedral structure, went through a phase transition to a cubic system, with *Pm-3m* space group.

Although the main perovskite structure was retained after reduction, the formation of additional reflections in the XRD patterns were observed. These correspond to a Ruddlesden Popper phase (A_2BO_4) similar to $(La,Sr)_{m+1}(Cr,Fe)_mO_{3m+1}$. This observed decomposition of the perovskite to Ruddlesden Popper phases in reducing environments is not unusual and has been reported for complex perovskite compositions with double A-site and B-site substitution.[31–33] According to the literature, the coexistence of an ABO_3, A_2BO_4 and A_2O_3 or BO phases is thermodynamically favourable.[31] In the case of these perovskites, the XRD patterns showed no indication of any other phase, such as A_2O_3 or BO to balance the formation of the A_2BO_4 phase. However, there is evidence in the literature that in LSCF the exsolution of Fe can take place.[15,34] So, if any Fe_2O_3 phase forms, it can be reduced to Fe^0. However, this would be below the detection limit of the XRD, due to the very low phase fraction.

Furthermore, the intensity of the peak corresponding to this A_2BO_4 phase decreased when the Ni doping increased, as presented in Figure 3. As explained above, when the Ni doping increased on the B-site of LSCF the Fe^{4+}/Fe^{3+} ratio increased, since Fe tends to obtain the +4 oxidation state, in order to compensate the charge balance. Thus, during

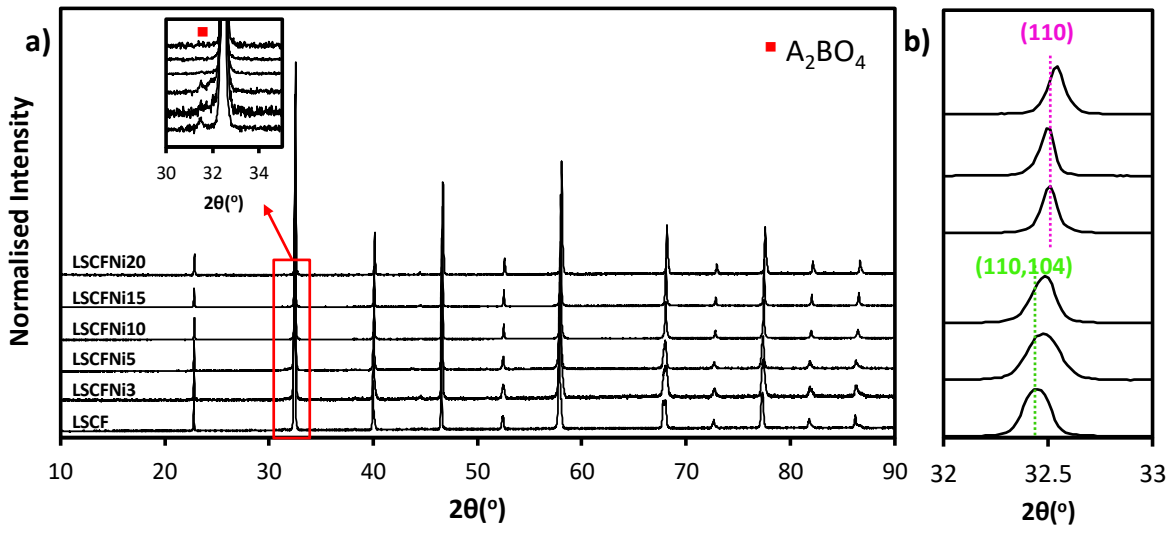

Figure 3 a) Post-reduction room temperature XRD of the LSCFNi perovskites b) Magnified section of the room temperature XRD patterns

Table 3 Post-reduction unit cell parameters of the LSCFNi perovskites

	LSCF	LSCFNi3	LSCFNi5	LSCFNi10	LSCFNi15	LSCFNi20
Space Group	*R-3c*	*R-3c*	*R-3c*	*Pm-3m*	*Pm-3m*	*Pm-3m*
***a* (Å)**	5.5224(17)	5.5178(15)	5.5186(10)	3.8949(3)	3.8909(1)	3.8866(1)
***c* (Å)**	13.485(4)	13.483(4)	13.483(4)	-	-	-
Volume (Å³)	356.16(21)	355.50(18)	355.60(8)	59.088(9)	58.906(3)	58.712(3)
Va (Å³)	59.36	59.25	59.26	59.09	58.91	58.71

reduction, Fe must undergo more transition steps from Fe^{4+} to Fe^0. As a result, less Fe^{2+}/Fe^0 species will form, and the formation of the A_2BO_4 phase will be less favourable.

Similar trends, but to the opposite direction, have been reported in the literature for the $(La_{0.75}Sr_{0.25})(Cr_{0.5}Mn_{0.5})O_3$ perovskite. More specifically, when La was substituted by Pr on the A-site, Mn obtained the Mn^{3+} oxidation state on the B-site and during reduction the decomposition to A_2BO_4 phase was more favourable, because the reduction of Mn^{3+} to Mn^{2+} was easier.[35]

Figure 3b presents the magnified area of the XRD patterns at 32-33 °. The (110,114) reflection of the samples that exhibited the rhombohedral structure and the (110) reflection of the samples with the cubic structure are illustrated. The change in the peak shape shows the change in the symmetry of the cell between 5 and 10 mol% doping, as explained earlier. In addition, these reflections show a shift to higher 2θ angles when the Ni doping increased. Therefore, even after reduction the cells with the higher Ni doping exhibited a smaller unit cell.

The cell parameters of the LSCFNi compounds after reduction are presented in Table 3. The pseudocubic cell volume was calculated, to compare the unit cell volume of the samples that exhibited different structures. As with the as-prepared samples, the unit cell volume decreased, when the level of Ni doping increased.

The XRD analysis of the $(La_{0.75}Sr_{0.25})(Cr_{0.5}Fe_{0.5-x}Ni_x)O_3$ compounds, as listed in Table 2 and Table 3, is summarised in Figure 4. It illustrates the relationship between the Ni doping and the pseudocubic cell volume before (black points) and after reduction (red points). As explained above, the unit cell volume of LSCF decreased, when the Ni doping increased, with similar trends observed before and after reduction. However, the relationship between the Ni doping and the pseudocubic cell volume was not linear. A change in the gradient of the trend line was observed, which is related to a change in the cell symmetry, from orthorhombic to rhombohedral for the as-prepared samples and from rhombohedral to cubic for the reduced samples. Therefore, by extrapolating the trendlines, it can be estimated that the change in the cell symmetry occurred with Ni doping of 7 mol%, approximately. Finally, this plot shows that for all the samples the cell volume increased after the reduction treatment. As explained above, during reduction Cr^{3+} remained stable and the Fe^{3+}/Fe^{4+} redox couple reduced to lower cation valences.[31,34] Since the ionic radius of Fe^{4+} (0.585Å) is smaller than that of Fe^{3+}(0.645Å) and Fe^{2+} (0.78Å), the cell expands during reduction.[29]

Thermal analysis

Thermogravimetric analysis in reducing environment. Thermogravimetric analysis was carried out for the LSCFNi compounds in 5% H_2/Ar up to 900 °C, to investigate the oxygen deficiency of the perovskites during reduction and the influence of the Ni doping on it. Figure 5a presents the weight change of the samples while heating up to 900 °C in 5% H_2/Ar. All the materials showed similar behaviour under reducing conditions. More specifically, weight loss took place in one main step between 380-500 °C (Figure S2), which corresponds to the loss of oxygen from the perovskite due to the reduction of the material. Based on TGA studies for similar perovskite structures, it is expected that these are the temperatures where phase transitions take place during the reduction of the perovskite.[34] According to Figure 5a, the samples with more Ni incorporated

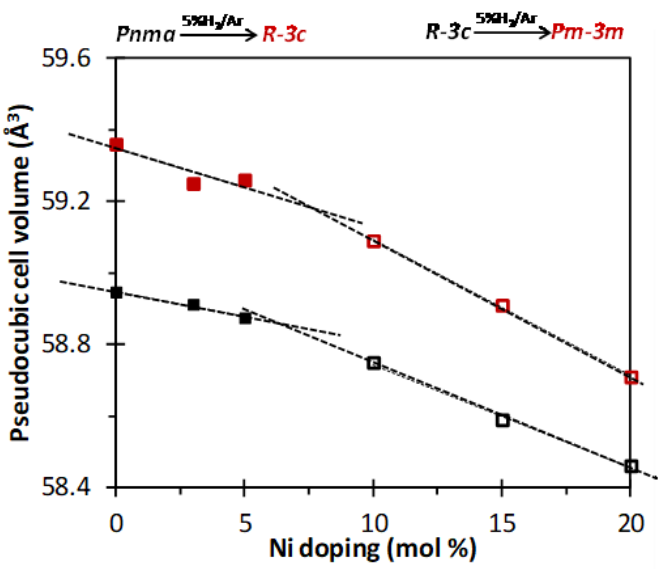

Figure 4 Relationship between Ni doping in the LSCFNi perovskites and the pseudocubic cell volume of the as-prepared (black points) and pre-reduced (red points) samples

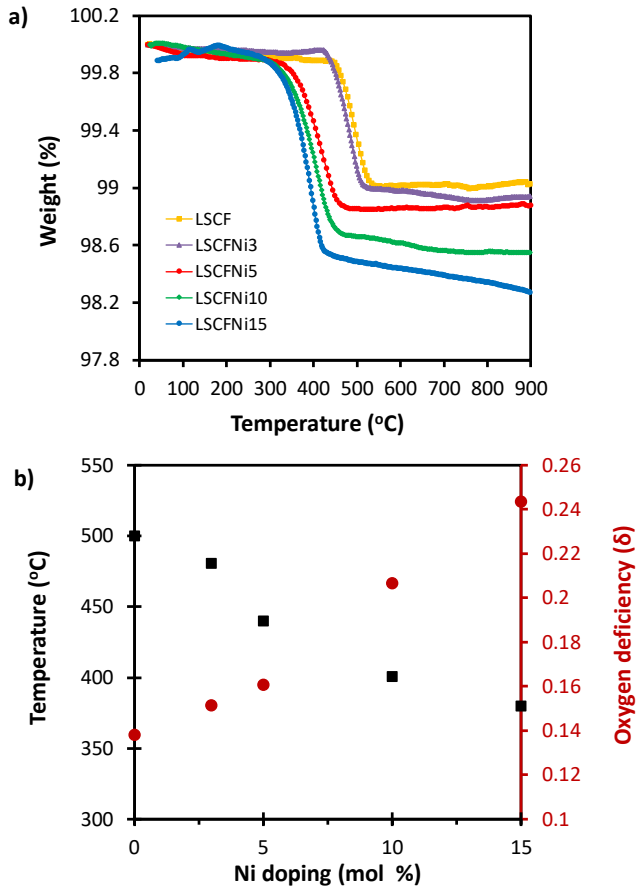

Figure 5 a) Thermogravimetric Analysis for the LSCF compounds in 5% H_2/Ar b) Relation between the Ni doping on LSCF and the reduction temperature and oxygen deficiency

on the B-site of LSCF showed greater mass losses on reduction. More specifically, LSCF lost 0.96% of its initial weight, which corresponds to 0.138 oxygen per formula unit. When the Ni doping increased up to 15 mol%, the perovskite lost 1.71% of its initial weight, which corresponds to 0.244 oxygen per formula unit. Additionally, when Ni was incorporated in LSCF the reduction temperature shifted to lower values, indicating that the Ni doping in LSCF increased the reducibility of the perovskite. Thus, the reduction temperature for LSCF was 500 °C and for LSCFNi15 decreased to 380 °C.

The TGA from this experiment is summarised in Figure 5b. It illustrates the relationship between the Ni doping in LSCF and the reduction temperature, as well as the oxygen deficiency of the perovskite during reduction. Obviously, by increasing the Ni doping in LSCF the oxygen deficiency of the perovskite during reduction gradually increased, while the reduction temperature decreased. However, this relationship was not linear. Two different regimes were evident, as observed with the XRD analysis (Figure 4) and can be attributed to the change in the symmetry of the cell from orthorhombic to rhombohedral.

According to the literature, when the reduction takes place in LSCF, Fe^{3+} and Fe^{4+} reduce to lower cation valences.[15,34] Cr^{3+} on the B-site of LSCF is stable during reduction and occupies the 6-fold coordination of the perovskites lattice.[15] In this study, when Ni was incorporated in the B-site of LSCF, Ni^{2+} can also reduce to Ni^0. The more Ni was incorporated into the lattice the more oxygen the perovskite lost and at lower temperatures, due to further reduction of the Ni^{2+} species. This can explain the higher oxygen deficiency of the perovskite, when the Ni doping in LSCF increased.

Assuming the difference in the observed weight loss of the LSCFNi compounds is attributed to the reduction of the extra Ni that was doped in the lattice, the amount of Ni that was reduced from the LSCFNi perovskites can be estimated. More specifically, LSCF lost 0.138 moles of oxygen, due to the reduction of Fe^{3+}/Fe^{4+} to lower cation valences. LSCFNi15 lost 0.244 moles of oxygen due to the reduction of Fe^{3+}/Fe^{4+} and the reduction of Ni^{2+}. The difference between these samples was 0.106 moles of oxygen. This is equivalent to the moles of Ni that reduced from Ni^{2+} to Ni^0, since every O^{2-} that the perovskite lost corresponds to one Ni^{2+} that reduced to Ni^0. Therefore, the moles of Ni^{2+} reduced to Ni^0 can be calculated.

Table 4 summarises the % weight loss, the calculated moles of oxygen (δ) that each perovskite lost during reduction and the estimated moles of Ni reduced from each perovskite. As described in Figure 5, the relationship between the oxygen deficiency and the Ni doping was not linear, due to the change in the cell symmetry. Therefore, LSCFNi3 and LSCFNi5, which exhibited an orthorhombic structure, only 50% of the Ni of the perovskite was reduced to Ni^0. On the other hand, LSCFNi10 and LSCFNi15 that exhibited a rhombohedral structure, 70% of the perovskite Ni was reduced to Ni^0. This indicates that since the rhombohedral structure exhibits a higher symmetry than the orthorhombic, it will further facilitate the formation of oxygen vacancies in the perovskite upon reduction.[36]

Thermogravimetric analysis in redox environment. The redox stability of these samples was investigated at 900 °C, to study the reversibility of the oxygen deficiency in the perovskite lattice that took place during reduction. The samples were heated up to 900 °C in air and during an isotherm at this temperature 5% H_2/Ar (R) and air (O) were introduced alternately. The materials were equilibrated for 2 h at each step and the process was repeated three times. The reoxidation process appeared to be faster than the reduction process and the perovskite recovered the initial oxygen content during the first few minutes of the reoxidation step (Figure S2). This suggests the oxygen diffusion was more favourable in the already reduced perovskite, due to the presence of oxygen vacancies in the structure. Figure 6 presents the calculated atomic oxygen of the LSCF samples during the redox cycling experiments at 900 °C.

Table 4 Summary of the TGA analysis in 5% H_2/Ar

Ni doping (mol)	Weight Loss (%)	Moles of oxygen, δ	Ni reduced (mol)
0	0.96	0.138	-
0.03	1.06	0.152	0.014
0.05	1.12	0.161	0.023
0.10	1.45	0.207	0.069
0.15	1.71	0.244	0.106

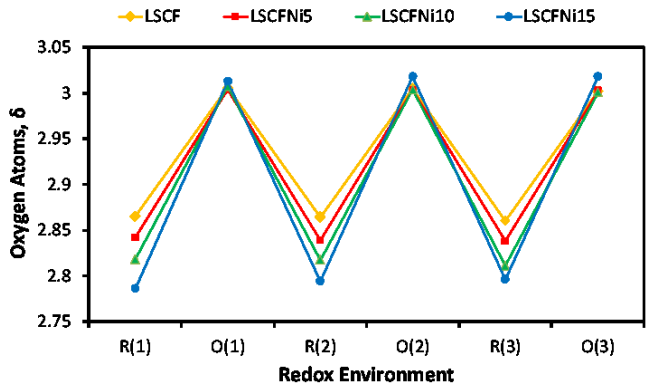

Figure 6 Calculated oxygen atoms per formula unit of the LSCFNi compounds during the TGA redox cycling experiments at 900 °C

According to this plot, all the tested compositions were very stable during redox cycling, and the achievable oxygen deficiency was reversible. Therefore, they demonstrated high redox tolerance, since they can reversibly lose and reincorporate oxygen in their structure.

Nanoparticles exsolution

The post-reduction SEM micrograph of LSCFNi15 is given in Figure 7a. This shows after annealing the sample in 5% H_2/Ar at 900 °C for 20 hr, the exsolution of metal nanoparticles took place on the surface of the perovskite. These nanoparticles were uniformly dispersed on the surface of LSCFNi15 and their average diameter was approximately 31 nm (Figure 7b). It is worth pointing out that no nanoparticle decoration was observed on the single phase LSCFNi15 perovskite before reduction (Figure S4).

Figure 7c shows the TEM micrograph of an exsolved metal nanoparticle on the surface of LSCFNi15. This nanoparticle was well-anchored on the surface of the perovskite by one third of its diameter. Similar observations have been reported in the literature for exsolved Ni nanoparticles from strontium titanates, suggesting that this strong interaction between the parent perovskite and the metal nanoparticle leads to enhanced thermal stability and coking resistance.[20]

EDX analysis performed suggests the exsolved nanoparticle from LSCFNi15 was an Fe-Ni alloy and the Fe:Ni ratio was 20:80 (Figure 7d). It has been reported in the literature before the exsolution of Fe from the LSCF perovskite, due to reduction of the Fe^{3+}/Fe^{4+} redox couple to Fe^0.[15,28] However, when Ni was incorporated in the structure, both Fe and Ni reduced simultaneously and formed an Fe-Ni solid solution. The exsolution of Fe-Ni alloy nanoparticles with various ratios from different perovskite structures has been reported in the literature before, confirming that the two elements exsolve as an alloy and not as two separate metals.[32,37,38] Therefore, in the case of the LSCFNi compounds the formation of bimetallic Fe-Ni nanocatalysts took place.

The exsolution of Fe-Ni alloy nanoparticles was observed for all the LSCFNi samples (Figure S5a, b). The average particle sizes were similar for the different perovskites and varied between 31-35 nm (Figure S5c, d). However, the EDX analysis suggests that for lower Ni doping the exsolved nanoparticles had lower Ni content and the Fe:Ni ratio was 35:65 (Figure S5g). Overall, for all the LSCFNi compounds the exsolved alloy nanoparticles were richer in Ni than Fe. This was because the Gibbs free energy of reduction of the NiO to Ni is lower than that of Fe_2O_3 to Fe, as it has been calculated by Neagu *et al.*[21] Therefore it was easier for the reduction of Ni^{2+} to Ni^0 to take place, than the reduction of Fe^{3+} to Fe^0.

Figure 7e, f presents the elemental mapping of the exsolved nanoparticle from the LSCFNi15. The distribution of Fe (light blue) and Ni (purple) was uniform in the area of the nanoparticle, confirming that they formed as an alloy. No oxygen was detected around the nanoparticle, indicating that both metals were fully reduced. Moreover, the signal for Ni was higher than the signal of Fe, since the alloy contained more Ni than Fe, as discussed above. The rest of the elements were uniformly distributed in the support area, which was the reduced LSCFNi15 perovskite.

Reduction mechanism

To summarise this analysis, a possible mechanism can be proposed for the reduction and exsolution of metal nanoparticles from the $(La_{0.75}Sr_{0.25})(Cr_{0.5}Fe_{0.5-x}Ni_x)O_3$ perovskites. During the reduction of the perovskite the

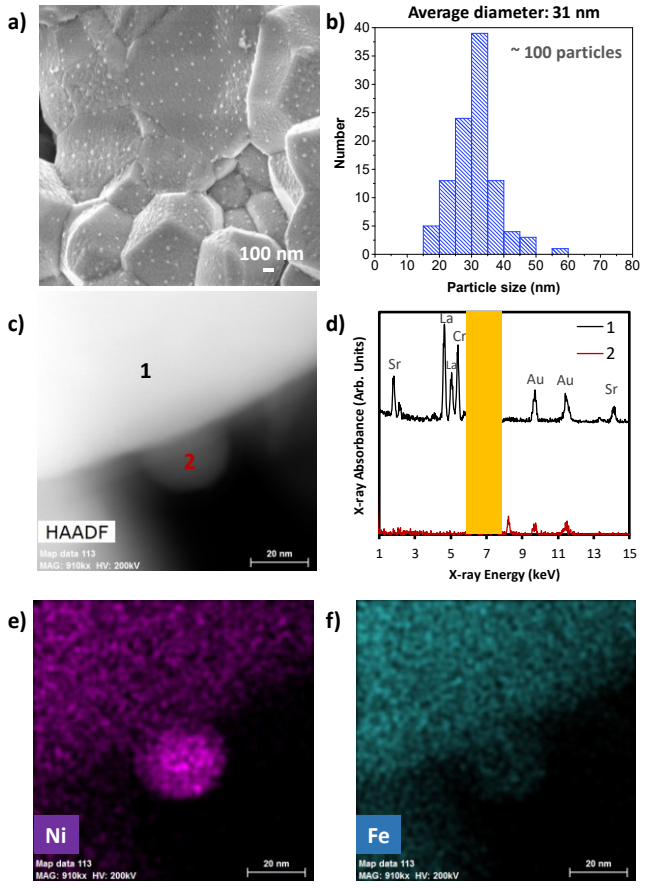

Figure 7 Exsolution of Fe-Ni alloy nanoparticles from LSCFNi15 a) SEM micrograph b) particle size histogram for the exsolved particles in a c) TEM micrograph of exsolved particle d) EDX spectra of the parent perovskite (1) and the exsolved particle (2) e) corresponding elemental mapping of the TEM micrograph for Ni f) corresponding elemental mapping of the TEM micrograph for Fe

exsolution of Fe-Ni alloy nanoparticles was accompanied by the formation of a Ruddlesden Popper phase. These two phases formed simultaneously, when the reduction of Fe^{3+}/Fe^{4+} and Ni^{2+} from the B-site of the perovskite took place. The Cr^{3+} species on the B-site of LSCF were stable. Therefore the expected phase was similar $(La,Sr)_{m+1}(Cr,Fe)_mO_{3m+1}$.

A general schematic diagram of this reaction for an ABO_3 perovskite is illustrated in Figure 8a. According to previous works,[21,26] when the exsolution from the B-site of a stoichiometric ABO_3 perovskite takes place, it is usually accompanied by the formation of A-site oxides. These A-site oxides (AO) in combination with the ABO_3 perovskite can form $A_{m+1}B_mO_{3m+1}$ Ruddlesden Popper phases. This composition can be also described as an A-site excess perovskite. Therefore, the perovskite balances the exsolution of nanoparticles from the B-site by the formation of these phases.

Similar phase transformations have been reported in the literature for double perovskites during exsolution. Du *et al.* studied the double perovskite $Sr_2FeMo_{0.65}Ni_{0.35}O_{6-\delta}$, which decomposed on reduction to the Ruddlesden–Popper phase $Sr_3FeMoO_{7-\delta}$, the $Sr(FeMo)O_{3-\delta}$ perovskite, and the $FeNi_3$ bimetallic alloy nanoparticle catalyst.[32] Liu *et al.* developed a $(Pr_{0.4}Sr_{0.6})_3(Fe_{0.85}Mo_{0.15})_2O_7$ Ruddlesden Popper phase with *in-situ* exsolution of Co-Fe alloy nanoparticles for CO_2, electrolysis by reducing the $(Pr_{0.4}Sr_{0.6})(Co_{0.2}Fe_{0.7}Mo_{0.1})O_{3-\delta}$ perovskite in $5\%H_2/N_2$ at 850 °C.[39] In general, the coexistence of ABO_3 and $A_{m+1}B_mO_{3m+1}$ can be observed in complex perovskite systems $(A_{1-x}A'_x)(B_{1-y-z}B'_yB''_z)O_3$, which undergo phase transformations in reducing environments.[34]

A schematic representation of the exsolution of Fe-Ni alloy nanoparticles from the $(La_{0.75}Sr_{0.25})(Cr_{0.5}Fe_{0.5-x}Ni_x)O_3$ perovskites is presented in Figure 8b. As illustrated, the starting material is a stoichiometric perovskite with the metal cations incorporated in the structure. During reduction, the exsolution of Fe-Ni alloy nanoparticles from the B-site takes place, leading to the formation of a Ruddlesden Popper phase similar to $(La,Sr)_{m+1}(Cr,Fe)_mO_{3m+1}$. The exsolution starts from areas close to the surface and as the perovskite keeps reducing the cation diffusion takes place from areas deeper from the structure.[18] Therefore, the $(La,Sr)_{m+1}(Cr,Fe)_mO_{3m+1}$ phase forms a shell around the perovskite particles.

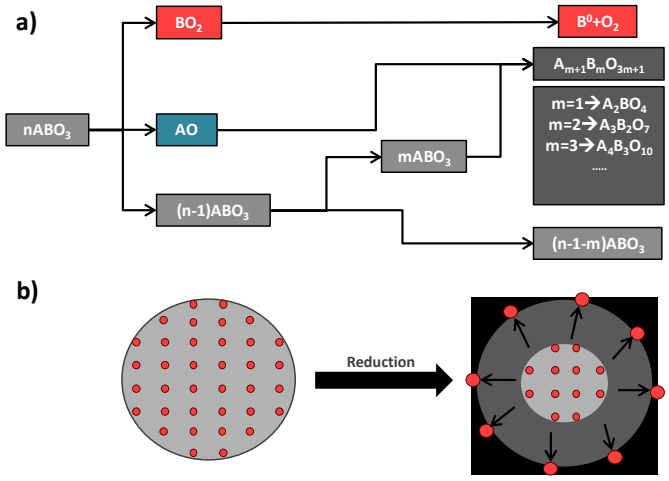

Figure 8 Illustration models for a) reaction mechanism and b) surface morphology evolution during the reduction of an ABO_3 perovskite, where the exsolution of metal nanoparticles is accompanied by the formation of a Ruddlesden Popper phase

Catalytic experiments

Figure 9a presents the gas composition from the outlet of the reactor after 20 h of testing with the catalysts, in comparison with the gas composition from the inlet of the reactor. According to the data, when LSCF was used as catalyst the CH_4 concentration did not change significantly. However, the CO_2 and H_2 concentrations decreased, while the CO and H_2O increased, indicating that the reverse-water gas shift reaction (Eq. 3) took place. By increasing the Ni content and incorporating the Fe-Ni alloy nanoparticles on the surface of LSCF, the CH_4 concentration gradually decreased. Moreover, by increasing the Ni doping, the CO_2, H_2O concentrations decreased, while the H_2 and CO increased, with a H_2/CO ratio between 2.3-2.5. This suggests that in parallel with the reverse-water gas shift reaction the methane steam reforming reaction also took place according to Eq. 1 and to a smaller extent, the methane dry reforming reaction (Eq. 2).

Figure 9b presents the evolution of the CH_4 conversion with time during 20 h of catalytic testing at 900 °C. LSCF exhibited a very low CH_4 conversion, which was stable with time. By increasing the Ni doping the CH_4 conversion increased, indicating that the Fe-Ni alloy nanoparticles are the active sites for the CH_4 consumption. Thus, by incorporating Ni in the structure of LSCF and with the exsolution of the Fe-Ni alloy nanoparticles, the activity of the perovskite increased regarding CH_4 conversion from 3.5% for LSCF to 72% for LSCFNi15. Moreover, after an initial equilibration time, all the materials demonstrated very good stability during the 20 h of testing, as no decrease in the CH_4 conversion was observed.

Figure 9c presents the evolution of the CO_2 conversion with time for all the catalysts. This diagram indicates that there was a small enhancement in the CO_2 conversion, when the Ni content increased. More specifically, LSCF demonstrated a CO_2 conversion of 72% and LSCFNi15 of 81%. This suggests that the Fe-Ni alloy nanoparticles did not contribute significantly to the CO_2 conversion, which took place from the reverse water-gas shift reaction. The additional CO_2 conversion for the Ni doped samples was due to the methane dry reforming reaction.

Figure 10 summarises the data collected during the catalytic testing of the LSCFNi catalysts and demonstrates the influence of Ni doping on CH_4 and CO_2 conversion. The values used for this graph were obtained at the end of the 20 h catalytic testing, when the materials were stabilised. According to this graph, by increasing the Ni doping on the LSCF perovskite the catalyst was more active regarding both CH_4 and CO_2 conversion, as discussed previously. However, the influence of Ni doping on the CH_4 conversion was more significant than on the CO_2 conversion. More specifically, LSCF demonstrated a CH_4 conversion of 3.5% while LSCFNi15 demonstrated 72%, enhancing the performance by a factor of 20. However, the CO_2 conversion of LSCF was 73% and of LSCFNi15 was 81%, which

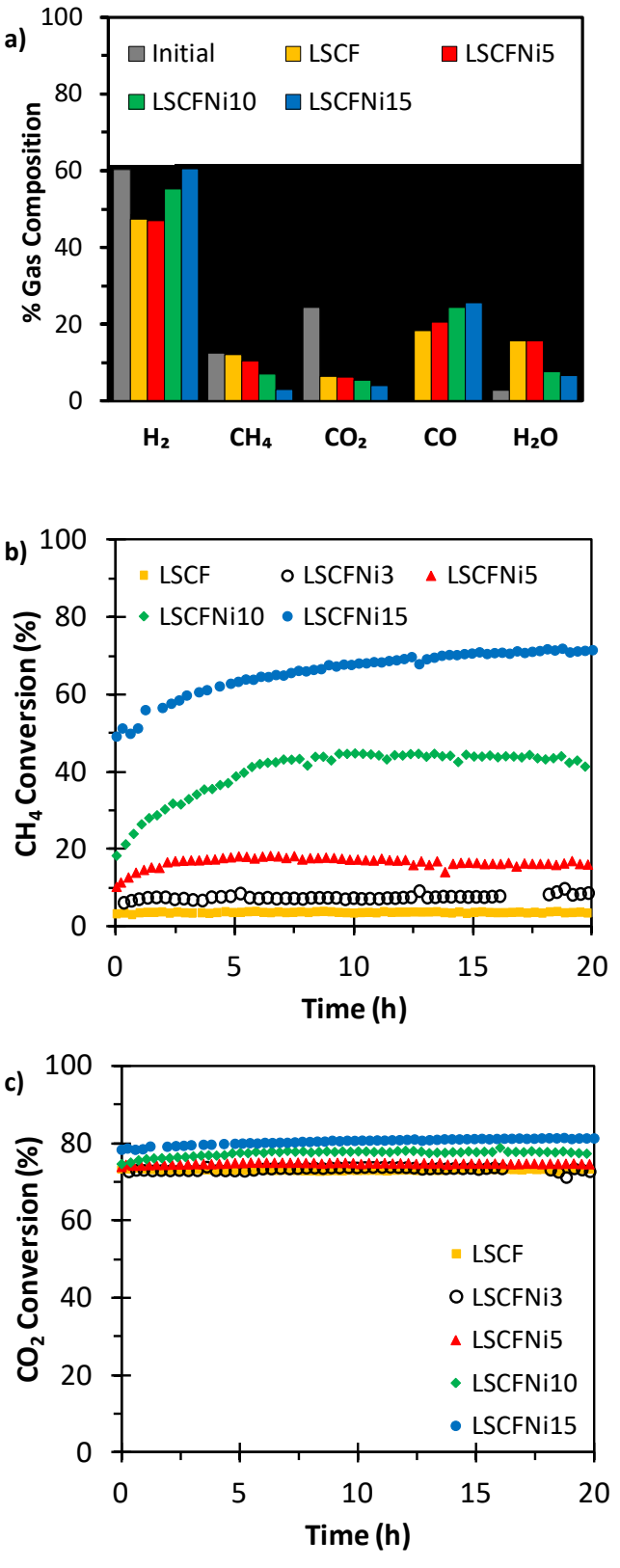

Figure 9 Catalytic testing for the LSCFNi perovskites at 900 °C a) Gas composition from the outlet of the reactor after 20 h testing b) Evolution of CH_4 conversion with time c) Evolution CO_2 conversion with time

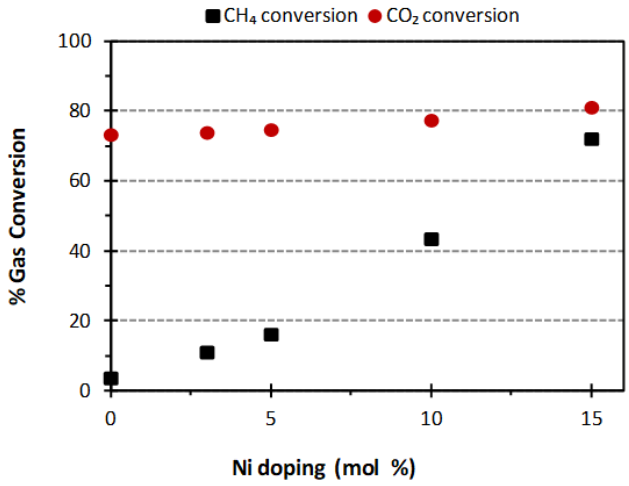

Figure 10 Relation between Ni doping on the LSCFNi perovskites and CH_4 and CO_2 conversion after 20 hr of testing at 900 °C

indicates just an enhancement of a factor of 1.12. These data strongly confirm that the active sites for the methane steam and dry reforming reactions are the Fe-Ni alloy nanoparticles, while the reverse water-gas shift reaction occurs at the perovskite backbone. In accordance to previous works,[40–42] the higher catalytic activity in the substituted perovskites can happen from the CO_2 adsorption on the perovskite backbone and the CH_4 dissociation on the metallic particles.

This increase in the performance of the perovskite can be explained based on the characterisation of the materials. More specifically, it was found that by increasing the Ni doping on the B-site of LSCF, the reducibility of the perovskite increased, as more Fe and Ni will reduce and the exsolution of metal nanoparticles will be further facilitated. Moreover, TEM-EDX analysis showed by increasing the level of Ni doping on the LSCF perovskite, the Fe:Ni ratio of the alloy nanoparticles changed from 35:65 to 20:80. This led to the greater catalytic activity of the LSCFNi perovskite regarding CH_4 conversion.

In addition, Figure 10 shows the relationship between the Ni doping and CH_4 conversion was not linear and demonstrated an interesting trend, which was similar to the trends presented in Figure 4 and Figure 5b for the cell volume and the oxygen deficiency of the LSCF perovskite during reduction. A change in the trend occurred for Ni doping of approximately 7 mol%, which was where the phase transition from the orthorhombic to rhombohedral system took place. As discussed before, by increasing the Ni doping on the B-site of LSCF, the oxygen deficiency of the perovskite during reduction increased and the exsolution of the Fe-Ni alloy nanoparticles was enhanced. This led to the improved activity of the perovskites regarding CH_4 conversion. Therefore, the different trends in the catalyst's performance in relation to the Ni doping, indicate that there was a strong correlation between the perovskite structure, the extent of the Fe-Ni alloy nanoparticles exsolution and the catalytic activity of the material regarding CH_4 conversion. Overall, the improved catalysts performance is a synergistic effect between the oxygen deficiency of the perovskite and the exsolution of Fe-Ni alloy nanoparticles during reduction.

Post-test catalyst characterisation

Post-test microstructure characterisation was performed on LSCFNi15. Figure 11a shows the SEM micrograph of LSCFNi15. After 20 h testing at 900 °C, the limited formation of carbon fibres around some of the exsolved nanoparticles was observed. These carbon fibres were short and grew in parallel with the perovskite surface, without uplifting the nanoparticle. This is the so-called "base growth" mechanism for the carbon fibre formation. It is typically observed for the exsolved nanoparticles, suggesting the interaction between the nanoparticle and the parent perovskite is strong.[20] Therefore, this did not affect the catalyst performance.

Figure 11b presents the particle size distribution of the exsolved nanoparticles after testing. The average particle size has increased from 31 (Figure 7b) to 46 nm. Moreover, the EDX line scan (Figure 11d) on the TEM micrograph of Figure 11c shows the formation of an oxygen layer around the nanoparticle of approximately 5 nm thickness. This can be also observed by the elemental mapping performed on this particle (Figure S6c). However, the nanoparticle remained well-anchored on the parent perovskite after 20 h testing. Finally, the EDX analysis on the nanoparticle showed a change on the Fe-Ni alloy composition from 20:80 to 10:90 (Figure S6b).

These results suggest that when the nanoparticles were exposed to the reaction gas mixture, morphological and compositional modifications took place. The increase of the particle size was attributed to a combination of particle oxidation during catalytic testing and rearrangement of the perovskite elements. Overall, due to the strong interaction between the exsolved nanoparticles and the parent perovskite, the nanoparticles can undergo transformations, but remain pinned on the surface.[43] Thus, these changes were not detrimental for the catalysts activity, which were stable over 20 h catalytic testing at 900 °C.

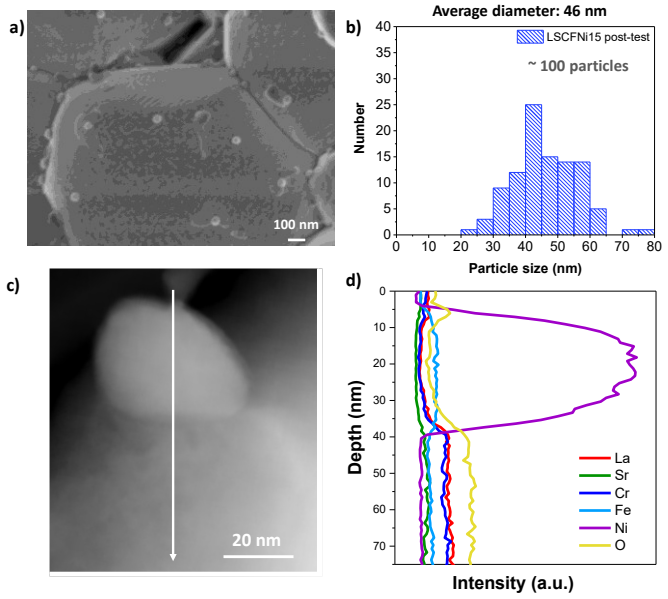

Figure 11 Post-test microstructure characterisation of LSCFNi15 a) SEM micrograph b) particle size histogram of the exsolved nanoparticles in a c) TEM micrograph of the exsolved nanoparticle d) line scan EDX of the TEM in c

Conclusions

In summary, the partial substitution of Fe by Ni in the $(La_{0.75}Sr_{0.25})(Cr_{0.5}Fe_{0.5-x}Ni_x)O_3$ perovskite was investigated and these materials were tested as potential catalysts for OTMs. The exsolution of Fe-Ni alloy nanoparticles was observed when the materials were exposed to a reducing environment. These nanoparticles significantly enhanced the catalytic activity of the parent perovskite for methane reforming reactions and were stable over 20 h testing. The optimum composition was the $(La_{0.75}Sr_{0.25})(Cr_{0.5}Fe_{0.35}Ni_{0.15})O_3$ perovskite, which demonstrated methane conversion of 72% and enhanced the activity over the initial perovskite by a factor of 20. Overall, by tuning the perovskite composition, it was possible to control the exsolution of the Fe-Ni alloy nanoparticles and consequently the activity of the catalysts for methane reforming. Therefore, these perovskites are promising candidate materials as catalysts for OTMs for methane reforming applications.

Conflicts of interest

There are no conflicts to declare.

Acknowledgements

The authors would like to thank Dr Jonathan Lane for helpful discussions and Praxair Inc for funding. We would also like to acknowledge support from EPSRC for Platform Grant EP/K015540/1 and EPSRC Capital for Great Technologies Grant EP/L017008/1.

Notes and references

1 1 E. T. Robinson, *Fuel Chem. Div.*, 2003, **48**, 347–349.
2 2 R. Anantharaman and O. Bolland, *Chem. Eng. Trans.*, 2011, 25–30.
3 3 L. Rosen, N. Degenstein, M. Shah, J. Wilson, S. Kelly, J. Peck and M. Christie, *Energy Procedia*, 2011, **4**, 750–755.
4 4 A. A. Yaremchenko, V. V. Kharton, A. A. Valente, S. A. Veniaminov, V. D. Belyaev, V. A. Sobyanin and F. M. B. Marques, *Phys. Chem. Chem. Phys.*, 2007, **9**, 2744–2752.
5 5 C. Zhang, X. Chang, X. Dong, W. Jin and N. Xu, *J. Memb. Sci.*, 2008, **320**, 401–406.
6 6 P. Zhang, X. F. Chang, Z. T. Wu, W. Q. Jin and N. P. Xu, *Ind. Eng. Chem. Res.*, 2005, **44**, 1954–1959.
7 7 W. Jin, C. Zhang, X. Chang, Y. Fan, W. Xing and N. Xu, *Environ. Sci. Technol.*, 2008, **42**, 3064–3068.
8 8 X. Chang, C. Zhang, Y. He, X. Dong, W. Jin and N. Xu, *Chinese J. Chem. Eng.*, 2009, **17**, 562–570.
9 9 A. Iulianelli, S. Liguori, J. Wilcox and A. Basile, *Catal. Rev.*, 2016, **4940**, 1–35.
10 10 A. Thursfield, A. Murugan, R. Franca and I. S. Metcalfe, *Energy Environ. Sci.*, 2012, **5**, 7421.
11 11 S. Hamakawa, K. Sato, T. Inoue, M. Nishioka, K. Kobayashi and F. Mizukami, *Catal. Today*, 2006, **117**, 297–303.
12 12 C. Delbos, G. Lebain, N. Richet and C. Bertail, *Catal. Today*, 2010, **156**, 146–152.
13 13 V. Sadykov, V. Zarubina, S. Pavlova, T. Krieger, G. Alikina, A. Lukashevich, V. Muzykantov, E. Sadovskaya, N. Mezentseva, E. Zevak, V. Belyaev and O. Smorygo, *Catal. Today*, 2010, **156**, 173–180.

14 14 A. Atkinson, S. Barnett, R. J. Gorte, J. T. S. Irvine, A. J. McEvoy, M. Mogensen, S. C. Singhal and J. Vohs, *Nat. Mater.*, 2004, **3**, 17–27.
15 15 S. Tao and J. T. S. Irvine, *Chem. Mater.*, 2004, **16**, 4116–4121.
16 16 A. S. Yu, J. Kim, T. S. Oh, G. Kim, R. J. Gorte and J. M. Vohs, *Appl. Catal. A Gen.*, 2014, **486**, 259–265.
17 17 S. P. Jiang, *Int. J. Hydrogen Energy*, 2012, **37**, 449–470.
18 18 J. T. S. Irvine, D. Neagu, M. C. Verbraeken, C. Chatzichristodoulou, C. Graves and M. B. Mogensen, *Nat. Energy*, 2016, **1**, 15014.
19 19 US Patent 7,556,676 B2, 2009.
20 20 D. Neagu, T.-S. Oh, D. N. Miller, H. Ménard, S. M. Bukhari, S. R. Gamble, R. J. Gorte, J. M. Vohs and J. T. S. Irvine, *Nat. Commun.*, 2015, **6**, 8120.
21 21 D. Neagu, G. Tsekouras, D. N. Miller, H. Ménard and J. T. S. Irvine, *Nat. Chem.*, 2013, **5**, 916–923.
22 22 T. Screen, *Platin. Met. Rev.*, 2007, **51**, 87–92.
23 23 H. Tanaka, M. Uenishi, M. Taniguchi, I. Tan, K. Narita, M. Kimura, K. Kaneko, Y. Nishihata and J. Mizuki, *Catal. Today*, 2006, **117**, 321–328.
24 24 J. Myung, D. Neagu, D. N. Miller and J. T. S. Irvine, *Nature*, 2016, **573**, 528–531.
25 25 G. Tsekouras, D. Neagu and J. T. S. Irvine, *Energy Environ. Sci.*, 2013, **6**, 256.
26 26 Y. Nishihata, J. Mizuki, T. Akao, H. Tanaka, M. Uenishi, M. Kimura, T. Okamoto and N. Hamada, *Nature*, 2002, **418**, 164–167.
27 27 Y. F. Sun, Y. Q. Zhang, J. Chen, J. H. Li, Y. T. Zhu, Y. M. Zeng, B. S. Amirkhiz, J. Li, B. Hua and J. L. Luo, *Nano Lett.*, 2016, **16**, 5303–5309.
28 28 Y. Li, Y. Wang, W. Doherty, K. Xie and Y. Wu, *ACS Appl. Mater. Interfaces*, 2013, **5**, 8553–62.
29 29 R. Shannon, *Acta Crystallogr.*, 1976, **32**, 751–767.
30 30 T. Jardiel, M. T. Caldes, F. Moser, J. Hamon, G. Gauthier and O. Joubert, *Solid State Ionics*, 2010, **181**, 894–901.
31 31 M. Kuhn, S. Hashimoto, K. Sato, K. Yashiro and J. Mizusaki, *Solid State Ionics*, 2011, **195**, 7–15.
32 32 Z. Du, H. Zhao, S. Yi, Q. Xia, Y. Gong, Y. Zhang, X. Cheng, Y. Li, L. Gu and K. Świerczek, *ACS Nano*, 2016, **10**, 8660–8669.
33 33 S. Sengodan, S. Choi, A. Jun, T. H. Shin, Y. W. Ju, H. Y. Jeong, J. Shin, J. T. S. Irvine and G. Kim, *Nat. Mater.*, 2015, **14**, 205–209.
34 34 E. Konysheva and J. T. S. Irvine, *Chem. Mater.*, 2009, **21**, 1514–1523.
35 35 E. S. Raj and J. T. S. Irvine, *Solid State Ionics*, 2010, **180**, 1683–1689.
36 36 D. Neagu and J. T. S. Irvine, *Chem. Mater.*, 2011, **23**, 1607–1617.
37 37 Y.-F. Sun, J.-H. Li, L. Cui, B. Hua, S.-H. Cui, J. Li and J.-L. Luo, *Nanoscale*, 2015, **3**, 11173–11181.
38 38 S. Liu, Q. Liu and J. L. Luo, *ACS Catal.*, 2016, **6**, 6219–6228.
39 39 S. Liu, Q. Liu and J.-L. Luo, *J. Mater. Chem. A*, 2016, **4**, 17521–17528.
40 40 G. C. de Araujo, S. M. de Lima, J. M. Assaf and M. A. Pena, *Catal. Today*, 2008, **133**–**135**, 129–135.
41 41 J. T. Richardson and S. A. Paripatyadar, *Appl. Catal.*, 1990, **61**, 293–309.
42 42 Z. Zhang and X. E. Verykios, *Appl. Catal. A*, 1996, **138**, 109–133.
43 43 D. Neagu, E. I. Papaioannou, W. K. W. Ramli, D. N. Miller, B. J. Murdoch, H. Ménard, A. Umar, A. J. Barlow, P. J. Cumpson, J. T. S. Irvine and I. S. Metcalfe, *Nat. Commun.*, 2017, **1855**, 1–8.